

Non-local Low-rank Cube-based Tensor Factorization for Spectral CT Reconstruction

Weiwen Wu, Fenglin Liu, Yanbo Zhang, *Senior Member, IEEE*, Qian Wang and Hengyong Yu, *Senior Member, IEEE*

Abstract—Spectral computed tomography (CT) reconstructs material-dependent attenuation images with the projections of multiple narrow energy windows, it is meaningful for material identification and decomposition. Unfortunately, the multi-energy projection dataset always contains strong complicated noise and result in the projections has a lower signal-noise-ratio (SNR). Very recently, the spatial-spectral cube matching frame (SSCMF) was proposed to explore the non-local spatial-spectrum similarities for spectral CT. The method constructs such a group by clustering up a series of non-local spatial-spectrum cubes. The small size of spatial patch for such a group make SSCMF fails to encode the sparsity and low-rank properties. In addition, the hard-thresholding and collaboration filtering operation in the SSCMF are also rough to recover the image features and spatial edges. While for all steps are operated on 4-D group, we may not afford such huge computational and memory load in practical. To avoid the above limitation and further improve image quality, we first formulate a non-local cube-based tensor instead of the group to encode the sparsity and low-rank properties. Then, as a new regularizer, Kronecker-Basis-Representation (KBR) tensor factorization is employed into a basic spectral CT reconstruction model to enhance the ability of extracting image features and protecting spatial edges, generating the non-local low-rank cube-based tensor factorization (NLCTF) method. Finally, the split-Bregman strategy is adopted to solve the NLCTF model. Both numerical simulations and realistic preclinical mouse studies are performed to validate and assess the NLCTF algorithm. The results show that the NLCTF method outperforms the other competitors.

Index Terms—spectral computed tomography (CT), image reconstruction, tensor factorization, Kronecker-Basis-Representation, non-local image similarity

I. INTRODUCTION

THE spectral computed tomography (CT) has obtain a great achievement in aspect of tissue characterization [1], lesion detection [2] and material decomposition [3], *etc.* Dual-

This work was supported in part by the National Natural Science Foundation of China (No. 61471070), National Instrumentation Program of China (No. 2013YQ030629), NIH/NIBIB U01 grant (EB017140) and China Scholarship Council (No. 201706050070).

W. W. Wu and F. L. Liu* (liufl@cqu.edu.cn) are with Key Lab of Optoelectronic Technology and Systems, Ministry of Education, Chongqing University, Chongqing 400044, China. Asterisk indicates corresponding author.

Y. B. Zhang, Qian Wang and H. Y. Yu*(E-mail: hengyong-yu@ieee.org) are with the Department of Electrical and Computer Engineering, University of Massachusetts Lowell, Lowell, MA 01854, USA.

energy CT (DECT) uses two different energy settings to discriminate the differentiation of materials component in terms of their energy-related attenuation characteristics [4]. Because the DECT only contains two different energy settings, which can be considered as a simplest spectral CT. However, DCT usually employs conventional detectors (i.e., energy-integrating detectors) so that its results are tarnished by beam hardening and spectral blurring. Besides, there are only two different energy source/detector pairs, which results in only two or three basic material maps can be accurately decomposed from projections. The photon-counting detectors (PCDs) illuminate the prospect of multi-energy CT in practical applications, which can measure the energy of each incident photon by recording pulse height [5]. Theoretically, compared with the conventional energy integrating detector, PCD can improve signal-to-noise ratio with dose reduction by accounting the number of income photons. However, the PCD has a different response to individual photon's energy, which can lead to spectral distortion including the charge sharing, K-escape, and fluorescence x-ray emission and pulse pileups. These can further result in spectral CT projection datasets are tarnished by complicated noises [6]. It is difficult to obtain higher signal-noise-ratio (SNR) projections and satisfied reconstructed spectral images. The high quality of reconstructed spectral images can be achieved with higher-powered PCD or superior spectral image reconstruction methods. In this work, we mainly focus on improving image quality by developing a more powerful reconstruction technique.

There are many similar attempts have been made. According to the prior knowledge used in reconstruction model, all of these efforts can fall into two categories: empirical-knowledge and prior-image-knowledge [7]. The empirical-knowledge based methods transform the spectral images into a unified and image-independent transformation domain, and then formulate a sparsity/low-rank reconstruction model incorporating an L_0 -norm, nuclear-norm or L_1 -norm of the transform coefficients. Considering the diversity of targets, different empirical-knowledge were employed, such as total variation (TV) [8], tensor-based nuclear norm [9], PRISM (prior rank, intensity and sparsity model) [10], piecewise linear tight frame transform [11], total nuclear variation (TVN) [12], the patch-based low-rank [13], tensor nuclear norm (TNN) with TV [14], structure tensor TV [15]. However, image similarities in non-local spatial space are usually ignored among these methods. Very recently, considering the non-local similarity within spatial-spectrum space, we proposed the SSCMF algorithm by stacking up a series of similar small cubes ($4 \times 4 \times 4$) to a 4-D group and then operate hard-thresholding and collaboration filtering on the group [7]. Since the length of the patches in a group is usually too small (for example, 4×4) to exactly characterize the sparsity and low-rank property. In

addition, the hard-thresholding and collaboration filtering operation are rough in image feature recovery and spatial edge protection. Finally, both hard-thresholding and collaboration filtering operation are operated on the formulated group, we may not afford such huge computational and memory load in practical.

The prior-image-knowledge based methods explore both image sparsity and similarity by constructing a redundant dictionary from high quality prior images. The dual-dictionary learning (DDL) method was applied to sparse-view spectral CT reconstruction [16]. Tensor dictionary learning (TDL) was introduced into the spectral CT reconstruction to explore the image similarity among different energy bins [17]. Considering the similar number of image gradient of different energy bins, the image gradient L_0 -norm was incorporated into the TDL (L_0 TDL) framework for sparse-view spectral CT reconstruction [18]. The spectral prior image constrained compressed sensing algorithm (spectral PICCS)[19], TV-TV and total variation spectral mean (TV-SM) methods [20] can be considered as another group of the prior-image-knowledge based methods, where a high quality image was treated as prior images to constrain the final solution. Both of the two groups need high quality prior images, which may not be obtained in practice. In addition, all of them ignore the similarities from single energy-channel image.

To handle the aforementioned issues, the non-local low-rank cube-based tensor (NLCT) is constructed rather than a 4D group to sufficiently explore the similarities and features within spatial-spectrum domain. Compared with the group formulation in SSCMF algorithm, NLCT unfolds a 2D spatial image patch as a column vector and then it becomes 3-order tensor. Tucker[21] and CP [22]decompositions are the two classic tensor decomposition techniques. Specifically, Tucker decomposition treats a tensor as an affiliation of the orthogonal bases along its all modes integrated by a core coefficient tensor, and CP factorizes a tensor as a summation of a series of rank-1 Kronecker bases. However, CP decomposition cannot well characterize the low-rank property of the tensor subspaces along its modes and Tucker decomposition usually fails to assess tensor sparsity with the volume of the core tensor [23, 24]. To address with this issue, Kronecker-Basis-Representation (KBR) measure was first proposed for multispectral image denoising and completion and obtain excellent results [23-25]. Recently, the KBR tensor decomposition was also applied to low-dose dynamic cerebral perfusion computed tomography reconstruction and achieve outstanding performance[26].

To overcome the aforementioned issues, here, we propose a non-local low-rank cube-based tensor factorization (NLCTF) technique to employ further explore the spatial-spectral sparsity and low-rank property for spectral CT. Compared with the previous SSCMF method, the NLCTF formulates cube-based tensor so that it can better explore the non-local spatial and spectral similarity of spectral images. The KBR tensor decomposition regularization has better outperformances in feature extraction, image edge preservation and noise suppression than the hard-thresholding and collaboration filtering in the SSCMF algorithm. The contributions are mainly summarized as following three aspects. First, considering the characters of spectral images, we creatively formulate non-local

low-rank cube-based tensor. Second, we sufficiently analyze the features of spectral images and employ the KBR regularization term to further explore the image low-rank and sparsity. Third, the split-Bregman technique is employed to solve the NLCTF model.

The rest of this paper is organized as follows. In section II, mathematic model is constructed and the solution of reconstruction method is also given. In section III, numerical simulations and real datasets experiments are designed and performed to validate and assess our proposed algorithm. In section IV, some related issues are discussed and then draw the conclusions.

II. MATHEMATIC METHOD AND MODEL

A. Kronecker-Basis-Representation Tensor Factorization

A tensor of N^{th} order can be denoted as $\mathcal{X} \in \mathcal{R}^{I_1 \times I_2 \times I_3 \times \dots \times I_N}$, the Kronecker-Basis-Representation (KBR) measure for a tensor \mathcal{X} can be read as:

$$m(\mathcal{X}) = \|\mathcal{C}\|_0 + \alpha \prod_{n=1}^N \text{rank}(\mathbf{X}_{(n)}), \quad (1)$$

where $\|\cdot\|_0$ represents the L_0 norm and $\mathcal{C} \in \mathcal{R}^{I_1 \times I_2 \times I_3 \times \dots \times I_N}$ is the core tensor of \mathcal{X} with higher order singular value decomposition (HOSVD). $\mathbf{X}_{(n)}$ represents the unfolding matrix with the mode- n . $\alpha > 0$ is a tradeoff parameter to balance the role of the two terms. The first term in (1) constrains the number of Kronecker bases for representing the target tensor, complying with intrinsic mechanism of the CP decomposition [22]. The second term inclines to regularize the low-rank property of the subspace spanned upon each tensor mode, which can be considered as the nonzero-cube in the core tensor space. The KBR measurement facilitates both inner sparsity of the core tensor \mathcal{C} and low-rank property of all tensor unfolding modes $\mathbf{X}_{(n)}\{n = 1, \dots, N\}$. Compared with the conventional tensor sparsity measures, i.e., CP and Tucker decompositions [21], the KBR has advantages in measuring the capacity of tensor space and unifying the traditional sparsity measures in case of 1-order and 2-order. Thus, it was proposed and applied to multispectral image denoising [23-25]and then obtained a great success in low-dose dynamic cerebral perfusion reconstruction [26].

Note that the Eq. (1) contains L_0 -norm and low-rank terms, which lead to the optimization problem hard to solve. Here, the KBR was relaxed as a log-sum form, Eq. (1) can be rewritten as

$$m(\mathcal{X}) = f(\mathcal{C}) + \alpha \prod_{n=1}^N f^*(\mathbf{X}_{(n)}), \quad (2)$$

where

$$f(\mathcal{C}) = \sum_{i_1, i_2, \dots, i_N}^{I_1, I_2, \dots, I_N} \left(\log(|c_{i_1, i_2, \dots, i_N}| + \epsilon) - \log(\epsilon) \right) / (-\log(\epsilon))$$

$$f^*(\mathbf{X}_{(n)}) = \sum_q \left(\log(\sigma_q(\mathbf{X}_{(n)}) + \epsilon) - \log(\epsilon) \right) / (-\log(\epsilon))$$

are two log-sum forms [23]. ϵ is a small positive number and $\sigma_q(\mathbf{X}_{(n)})$ defines the q^{th} singular value of $\mathbf{X}_{(n)}$. In this work, we employ this relaxation form to approximate KBR measure.

B. Spectral CT imaging model

Considering the noisy projection datasets, the conventional CT forward model for fan-beam scanning geometry can be discretized as a linear system

$$\mathbf{y} = \mathbf{H}\mathbf{x} + \boldsymbol{\eta} \quad , \quad (3)$$

where $\mathbf{x} \in \mathcal{R}^N$ ($N = N_W \times N_H$) represents the vectorized 2D image. $\mathbf{y} \in \mathcal{R}^J$ ($J = J_1 \times J_2$) stands for the vectorized projections, J_1 and J_2 are respectively the view and detector numbers and $\boldsymbol{\eta} \in \mathcal{R}^J$ stands for projection noise. $\mathbf{H} \in \mathcal{R}^{J \times N}$ is the CT system matrix. Since the matrix \mathbf{H} is usually huge beyond the memory limitation, Eq. (3) can not be solved directly by a matrix inverse technique. Alternatively, it can be iteratively solved by minimizing the following optimization problem

$$\operatorname{argmin}_{\mathbf{x}} \frac{1}{2} \|\mathbf{y} - \mathbf{H}\mathbf{x}\|_2^2 \quad , \quad (4)$$

where $\|\cdot\|_2$ represents L_2 norm. Here, Eq. (4) becomes a linear programming problem and it can be updated with the ART or SART methods [27]. To further optimize the solution, a regularization of prior knowledge can be introduced into Eq. (4). Therefore, we have

$$\operatorname{argmin}_{\mathbf{x}} \frac{1}{2} \|\mathbf{y} - \mathbf{H}\mathbf{x}\|_2^2 + \lambda R(\mathbf{x}) \quad . \quad (5)$$

The Eq. (5) contains two terms, i.e., data fidelity term $\frac{1}{2} \|\mathbf{y} - \mathbf{H}\mathbf{x}\|_2^2$ and regularization term $R(\mathbf{x})$, and $\lambda > 0$ is a comprised parameter between the data fidelity and regularization terms.

For the spectral CT, the emitted x-ray spectrum is divided into several narrow energy channels, the detectors can collect multiple projection datasets of the imaged object with one scan. Each projection dataset can reconstruct energy-dependent image. Therefore, the model of spectral CT reconstruction can be expressed as following

$$\operatorname{argmin}_{\mathbf{x}} \sum_{s=1}^S \frac{1}{2} \|\mathbf{y}_s - \mathbf{H}\mathbf{x}_s\|_2^2 + \lambda R(\mathbf{X}) \quad , \quad (6)$$

where \mathbf{x}_s is the s^{th} ($s = 1, 2, \dots, S$) energy channel vectorized image and $\mathbf{X} \in \mathcal{R}^{N_W \times N_H \times S}$ is a 3rd-order tensor representing a set of $\{\mathbf{x}_s\}_{s=1}^S$. \mathbf{y}_s is the s^{th} energy channel projection.

The most significant issue of recovering spectral CT images from its projections is to rationally extract prior structure knowledge under a to-be-reconstructed images, and fully utilize such prior information to regularize reconstruction model. Due to the advantages of KBR regularizer, in this work, KBR prior is incorporated into spectral CT reconstruction, i.e., the $R(\mathbf{X})$ is replaced with the aforementioned $m(\mathbf{X})$. Eq. (6) can be rewritten as

$$\operatorname{argmin}_{\mathbf{x}} \sum_{s=1}^S \frac{1}{2} \|\mathbf{y}_s - \mathbf{H}\mathbf{x}_s\|_2^2 + \lambda m(\mathbf{X}) \quad . \quad (7)$$

C. Non-local similar cubes matching

The charge sharing, K-escape, and fluorescence x-ray emission and re-absorption cause severe noises in multi-energy projections, it can further compromise reconstructed images quality. To further effective implement image reconstruction, it requires to explore more prior knowledge. In this work, we mainly focus on the following three aspects. First, patients

usually only consist of two or three basic materials, i.e., soft tissue, bone and water in clinical application. The number of basic materials is less than energy channels. It indicates the spectral CT images contain a large amount of spectral redundancy and the images obtained across the spectrum are generally correlated. Second, as the multi-energy projection datasets are gathered from the same patient by using different energy threshold value, images reconstructed across spectral dimension have different attenuation coefficients and but share similar image structure information. Third, it is the fact that the small patches among different location share similar structure information in a single channel. These have been shown that such prior knowledge are very helpful for spectral CT reconstruction in our latest work [7]. To explore these prior knowledge and preserve horizontal and vertical structures, we extracted a series of non-local similar cubes around the current cube to construct a 4-D group. Fig. 1 demonstrates the process of grouping [7]. We can see that the length of the patches in spatial domain is usually too small (usually significantly small than the nonlocal similar cubes, i.e., 4×4) for the HOSVD to exactly extract the intrinsic subspace bases of the spatial information. While for comparative large length of the patches in spatial horizontal and vertical model, we can not afford such huge computational and memory load.

Therefore, in this work, we construct the 3-order low-rank tensor for recovery. Fig. 1 also illustrates how to construct the 3-order tensor. For one given cubic with size $r_w \times r_h \times r_s$ within the whole 3-D images, we search t similar non-local cubes in a given local window. Then, these extracted $t + 1$ small cubes can formulate a new 3-order tensor with the size of $(r_w r_h) \times r_s \times (t + 1)$, where $(r_w r_h) \times r_s$ is the matrix formation of cube and t is the number of the non-local similar cubes. The formatted 3-order tensor simultaneously explore the spatial local sparsity (mode-1), the non-local similarity among spectral-spatial cubes (mode-2) and spectral high correlation (mode-3), which would be good for tensor recovery using this unified framework. The constructed tensor format also provides a unified interpretation for the matrix-based recovery model. Especially, $r_s = 1$ or $t = 0$, the constructed 3rd tensor can be degenerated into a matrix by taking only non-local self-similarity or spectral correlation.

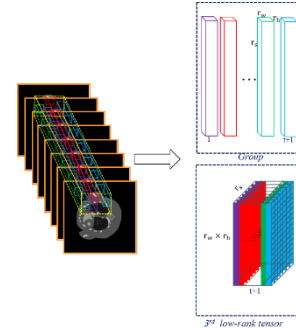


Fig.1 The formation process of a group and 3-order tensor.

Note that the number of energy channels usually is small in clinical application, r_s set as S in the 3rd low-rank tensor construction. By sweeping all across the spectral images with overlaps, we can build a set of 2D patches $\{\mathcal{G}_{ij}\}_{1 \leq i \leq N_W - r_w, 1 \leq j \leq N_H - r_h} \subset \mathcal{R}^{(r_w r_h) \times S}$ to represent the spectral CT images, where each energy channel of a small patch is ordered lexicographically as a column vector. We can now

reformulate all 2D patches as a group of $\{\mathbf{X}_l\}_{l=1}^L$, where $L = (N_W - r_w + 1) \times (N_H - r_h + 1)$ represents the number of patches over the whole spectral images. Furthermore, for a given current X_l , we can find $t(t \geq 1)$ patches similar to it within a non-local window. A low-rank 3-order tensor can be denoted as $\mathbf{X}_l \in \mathcal{R}^{(r_w r_h) \times S \times (t+1)}$. We call such a low-rank 3-order tensor as a cluster. Each small tensor can be considered as adding extraction operation E_l on original 3-order tensor \mathbf{X} . Here, \mathbf{X}_l can be furtherly expressed as

$$\mathbf{X}_l = E_l \mathbf{X} . \quad (8)$$

D. NLCTF reconstruction model

Considering the image itself non-local spatial similarity and correlation across spectral dimension and combining the KBR-based reconstruction model in Eq. (7), we now construct KBR-based non-local spectral CT reconstruction model. It can be established as follows

$$\operatorname{argmin}_{\mathbf{X}} \sum_{s=1}^S \frac{1}{2} \|\mathbf{y}_s - \mathcal{H} \mathbf{x}_s\|_2^2 + \lambda \sum_{l=1}^L m(\mathbf{X}_l) . \quad (9)$$

Substituting Eq. (8) into (9), we have

$$\operatorname{argmin}_{\mathbf{X}} \sum_{s=1}^S \frac{1}{2} \|\mathbf{y}_s - \mathcal{H} \mathbf{x}_s\|_2^2 + \lambda \sum_{l=1}^L m(E_l \mathbf{X}) . \quad (10)$$

To solve the optimization problem (10), split-Bregman method is employed. Now we split the \mathbf{X} and $E_l \mathbf{X}$ by introducing L auxiliary tensors $\{\mathcal{T}_l\}_{l=1}^L$ instead of $\{E_l \mathbf{X}\}_{l=1}^L$, Eq. (10) can be involved into following expression

$$\operatorname{argmin}_{\mathbf{X}} \frac{1}{2} \sum_{s=1}^S \|\mathbf{y}_s - \mathcal{H} \mathbf{x}_s\|_2^2 + \lambda \sum_{l=1}^L m(\mathcal{T}_l) ,$$

s. t. $\mathcal{T}_l = E_l \mathbf{X} \quad (l = 1, \dots, L)$ (11)

$$\mathbf{x}_{n_w n_h s}^{(k+1)} = \mathbf{x}_{n_w n_h s}^{(k)} - \beta [\mathcal{H}^T (\mathcal{H} \mathbf{x}_s^{(k)} - \mathbf{y}_s)]_{n_w n_h s} - \mu \left[\sum_{l=1}^L E_l^T (E_l \mathbf{x}^{(k)} - \mathcal{T}_l^{(k)} + \mathbf{w}_l^{(k)}) \right]_{n_w n_h s} . \quad (14)$$

where the symbols $[\cdot]_{n_w n_h} (1 \leq n_w \leq N_W, 1 \leq n_h \leq N_H)$ and $[\cdot]_{n_w n_h s}$ indicate the $(n_w, n_h)^{th}$ and $(n_w, n_h, s)^{th}$ element index within a matrix and a tensor respectively. $\beta \in (0, 2)$ is a relaxation factor, which set as 0.03 in our experiments [7]. Eq. (13c) can be easily solved using the steepest descent method

$$\mathbf{w}_l^{(k+1)} = \mathbf{w}_l^{(k)} - (\mathcal{T}_l^{(k+1)} - E_l \mathbf{x}^{(k+1)}), \forall l = 1, \dots, L \quad (15)$$

Now, the challenge is to solve the problem (13b). Substituting Eq. (2) into Eq. (13b), then we have

$$\operatorname{argmin}_{\{\mathcal{T}_l\}_{l=1}^L} \sum_{l=1}^L \left(f(\mathcal{C}_l) + \alpha \prod_{n=1}^3 f^*(\mathbf{T}_{l(n)}) \right) + \frac{\delta}{2} \sum_{l=1}^L \|\mathcal{T}_l - E_l \mathbf{x}^{(k+1)} - \mathbf{w}_l^{(k)}\|_F^2 , \quad (16)$$

where $\mathbf{T}_{l(n)}$ represents the unfolding matrix with the mode- n of the tensor \mathcal{T}_l . $\delta = \mu/\lambda$ and $N = 3$. It can be seen that Eq. (16) can be divided into L independent sub-problems

$$\operatorname{argmin}_{\mathcal{T}_l} f(\mathcal{C}_l) + \alpha \prod_{n=1}^3 f^*(\mathbf{T}_{l(n)}) + \frac{\delta}{2} \|\mathcal{T}_l - E_l \mathbf{x}^{(k+1)} - \mathbf{w}_l^{(k)}\|_F^2 . \quad (17)$$

Eq. (11) is a constrained linear program optimization problem, which can be furtherly converted into an unconstrained one

$$\operatorname{argmin}_{\mathbf{x}, \{\mathcal{T}_l, \mathbf{w}_l\}_{l=1}^L} \frac{1}{2} \sum_{s=1}^S \|\mathbf{y}_s - \mathcal{H} \mathbf{x}_s\|_2^2 + \lambda \sum_{l=1}^L m(\mathcal{T}_l) + \frac{\mu}{2} \sum_{l=1}^L \|\mathcal{T}_l - E_l \mathbf{x} - \mathbf{w}_l\|_F^2 . \quad (12)$$

where the Frobenius norm of a tensor is used. It can be denoted as $\|\mathcal{A}\|_F = (\sum_{i_1, i_2, \dots, i_N=1}^{I_1, I_2, \dots, I_N} a_{i_1, i_2, \dots, i_N}^2)^{1/2}$, a_{i_1, i_2, \dots, i_N} represents an element of the tensor \mathcal{A} . μ is the coupling parameter and $\{\mathbf{w}_l\}_{l=1}^L$ represent L error feedback tensors. Eq. (12) can be equivalent to the following three sub-problems:

$$\operatorname{argmin}_{\mathbf{x}} \left\{ \begin{array}{l} \frac{1}{2} \sum_{s=1}^S \|\mathbf{y}_s - \mathcal{H} \mathbf{x}_s\|_2^2 + \\ \frac{\mu}{2} \sum_{l=1}^L \|\mathcal{T}_l^{(k)} - E_l \mathbf{x} - \mathbf{w}_l^{(k)}\|_F^2 \end{array} \right\} , \quad (13a)$$

$$\min_{\{\mathcal{T}_l\}_{l=1}^L} \lambda \sum_{l=1}^L m(\mathcal{T}_l) + \frac{\mu}{2} \sum_{l=1}^L \|\mathcal{T}_l - E_l \mathbf{x}^{(k+1)} - \mathbf{w}_l^{(k)}\|_F^2 , \quad (13b)$$

$$\operatorname{argmin}_{\{\mathbf{w}_l\}_{l=1}^L} \frac{\mu}{2} \sum_{l=1}^L \|\mathcal{T}_l^{(k+1)} - E_l \mathbf{x}^{(k+1)} - \mathbf{w}_l\|_F^2 . \quad (13c)$$

where k is the current iteration number and Eqs. (13a) – (13c) can be alternately solved. Here, Eq. (13a) can be solved utilizing gradient descent. Its solution can be given by the following Eq. (14)

$$\operatorname{argmin}_{\mathbf{x}} \frac{1}{2} \sum_{s=1}^S \|\mathbf{y}_s - \mathcal{H} \mathbf{x}_s\|_2^2 + \lambda \sum_{l=1}^L m(\mathcal{T}_l) + \frac{\mu}{2} \sum_{l=1}^L \|\mathcal{T}_l - E_l \mathbf{x} - \mathbf{w}_l\|_F^2 . \quad (12)$$

To minimize the similar objective function in Eq. (17), the alternative alternating direction method of multipliers (ADMM) method was proposed [23]. Here, we adopt the split-Bregman method instead of ADMM to obtain the solution. Firstly, we need to introduce $3L$ auxiliary tensors $\mathcal{M}_{l_n} (n = 1, 2, 3)$. Eq. (17) can be written as

$$\operatorname{argmin}_{\mathcal{M}_{l_n}, \mathcal{C}_l, \mathbf{Q}_{l_n}} f(\mathcal{C}_l) + \alpha \prod_{n=1}^3 f^*(\mathbf{M}_{l(n)}) + \frac{\delta}{2} \|\mathcal{C}_l \times_1 \mathbf{Q}_{l_1} \times_2 \mathbf{Q}_{l_2} \times_3 \mathbf{Q}_{l_3} - E_l \mathbf{x}^{(k+1)} - \mathbf{w}_l^{(k)}\|_F^2$$

s. t. , $\mathcal{C}_l \times_1 \mathbf{Q}_{l_1} \times_2 \mathbf{Q}_{l_2} \times_3 \mathbf{Q}_{l_3} = \mathcal{M}_{l_n}$,

$$\mathbf{Q}_{l_n}^T \mathbf{Q}_{l_n} = \mathbf{I}, \forall n = 1, 2, 3 . \quad (18)$$

where the factor matrices $\mathbf{Q}_{l_n} (n = 1, 2, 3)$ denote orthogonal in columns and $\mathbf{M}_{l(n)}$ represent the unfolding matrix along mode- n of the tensor \mathcal{M}_{l_n} . Eq. (18) is a constrained problem which can be converted into an unconstrained problem

$$\begin{aligned} & \underset{\mathcal{M}_{l_n}, \mathbf{c}_l, \mathbf{Q}_{l_n}, \mathbf{Z}_{l_n}}{\operatorname{argmin}} f(\mathbf{C}_l) + \alpha \prod_{n=1}^3 f^*(\mathbf{M}_{l_n(n)}) \\ & + \frac{\delta}{2} \|\mathbf{c}_l \times_1 \mathbf{Q}_{l_1} \times_2 \mathbf{Q}_{l_2} \times_3 \mathbf{Q}_{l_3} - E_l \mathbf{X}^{(k+1)} - \mathbf{W}_l^{(k)}\|_F^2 \\ & + \frac{\theta}{2} \sum_{n=1}^3 \|\mathbf{c}_l \times_1 \mathbf{Q}_{l_1} \times_2 \mathbf{Q}_{l_2} \times_3 \mathbf{Q}_{l_3} - \mathcal{M}_{l_n} + \mathbf{Z}_{l_n}\|_F^2. \end{aligned} \quad (19)$$

where \mathbf{Z}_{l_n} represent error feedback tensor, θ is a positive parameter and \mathbf{Q}_{l_n} ($n = 1, 2, 3$) satisfy $\mathbf{Q}_{l_n}^T \mathbf{Q}_{l_n} = \mathbf{I}$. Now the Eq. (19) can be updated by solving following sub-problem:

i) \mathbf{c}_l sub-problem: With the other parameters fixed, \mathbf{c}_l can be updated by solving the following minimization problem:

$$\min_{\mathbf{c}_l} \gamma f(\mathbf{c}_l) + \frac{1}{2} \|\mathbf{c}_l \times_1 \mathbf{Q}_{l_1}^{(k)} \times_2 \mathbf{Q}_{l_2}^{(k)} \times_3 \mathbf{Q}_{l_3}^{(k)} - \mathcal{B}_l^{(k)}\|_F^2, \quad (20)$$

where $\gamma = 1/(\delta + 3\theta)$ and $\mathcal{B}_l^{(k)} = (\delta(E_l \mathbf{X}^{(k+1)} + \mathbf{W}_l^{(k)}) + \theta(\sum_{n=1}^3 (\mathcal{M}_{l_n}^{(k)} - \mathbf{Z}_{l_n}^{(k)}))) / (\delta + 3\theta)$. From [23], Eq. (20) can be furtherly converted to

$$\min_{\mathbf{c}_l} \gamma f(\mathbf{c}_l) + \frac{1}{2} \|\mathbf{c}_l - \mathcal{D}_l^{(k)}\|_F^2, \quad (21)$$

where

$$\mathcal{D}_l^{(k)} = \mathcal{B}_l^{(k)} \times_1 (\mathbf{Q}_{l_1}^{(k)})^T \times_2 (\mathbf{Q}_{l_2}^{(k)})^T \times_3 (\mathbf{Q}_{l_3}^{(k)})^T.$$

Eq. (21) has the closed-form solution given as following[28]

$$\mathbf{c}_l^{(k+1)} = D_{\gamma, \epsilon}(\mathcal{D}_l^{(k)}), \quad (22)$$

where $D_{\gamma, \epsilon}(\cdot)$ denote the hard-thresholding operation, which has the following form

$$D_{\gamma, \epsilon}(x) = \begin{cases} 0 & \text{if } |x| \leq 2\sqrt{c_1\gamma} - \epsilon \\ \operatorname{sign}\left(\frac{c_2(x) + c_3(x)}{2}\right) & \text{if } |x| > 2\sqrt{c_1\gamma} - \epsilon \end{cases}, \quad (23)$$

where $c_1 = (-1)/\log(\epsilon)$, $c_2(x) = |x| - \epsilon$, $c_3(x) = \sqrt{(|x| + \epsilon)^2 - 4c_1\gamma}$ and sign represents the sign function.

ii) \mathbf{Q}_{l_n} ($n = 1, 2, 3$) sub-problem: with respect to \mathbf{Q}_{l_1} , we fix the $\mathbf{Q}_{l_2}^{(k)}$, $\mathbf{Q}_{l_3}^{(k)}$ and others parameters. \mathbf{Q}_{l_1} can be updated by minimizing the following problem

$$\begin{aligned} \min_{\mathbf{Q}_{l_1}} & \frac{1}{2} \|\mathbf{c}_l^{(k+1)} \times_1 \mathbf{Q}_{l_1} \times_2 \mathbf{Q}_{l_2}^{(k)} \times_3 \mathbf{Q}_{l_3}^{(k)} - \mathcal{B}_l^{(k)}\|_F^2 \\ \text{s. t.} & (\mathbf{Q}_{l_1})^T \mathbf{Q}_{l_1} = \mathbf{I}, \end{aligned} \quad (24)$$

Refer to Zeng's work [26], Eq. (24) is equivalent to

$$\max_{(\mathbf{Q}_{l_1})^T \mathbf{Q}_{l_1} = \mathbf{I}} \langle \mathcal{L}_{l_1}, \mathbf{Q}_{l_1} \rangle, \quad (25)$$

where $\mathcal{L}_{l_1} = \mathbf{B}_{l_{(1)}}^{(k)} (\mathbf{Q}_{l_2}^{(k)} \otimes \mathbf{Q}_{l_3}^{(k)}) (\mathbf{c}_l^{(k+1)})^T$ and $\mathbf{B}_{l_{(1)}}^{(k)}$ represent the unfolding matrix of $\mathcal{B}_l^{(k)}$ along mode-1. The \mathbf{Q}_{l_1} can be updated by [23]

$$\mathbf{Q}_{l_1}^{(k+1)} = \mathbf{G}_{l_1} (\mathbf{V}_{l_1})^T, \quad (26)$$

where $\mathbf{G}_{l_1} \mathbf{\Theta}_{l_1} (\mathbf{V}_{l_1})^T$ represents the SVD decomposition of \mathcal{L}_{l_1} . In a similar way, \mathbf{Q}_{l_2} and \mathbf{Q}_{l_3} can be updated by minimizing Eq. (27)

$$\begin{cases} \min_{(\mathbf{Q}_{l_2})^T \mathbf{Q}_{l_2} = \mathbf{I}} \frac{1}{2} \|\mathbf{c}_l^{(k+1)} \times_1 \mathbf{Q}_{l_1}^{(k+1)} \times_2 \mathbf{Q}_{l_2} \times_3 \mathbf{Q}_{l_3}^{(k)} - \mathcal{B}_l^{(k)}\|_F^2 \\ \min_{(\mathbf{Q}_{l_3})^T \mathbf{Q}_{l_3} = \mathbf{I}} \frac{1}{2} \|\mathbf{c}_l^{(k+1)} \times_1 \mathbf{Q}_{l_1}^{(k+1)} \times_2 \mathbf{Q}_{l_2}^{(k+1)} \times_3 \mathbf{Q}_{l_3} - \mathcal{B}_l^{(k)}\|_F^2 \end{cases}. \quad (27)$$

iii) \mathcal{M}_{l_n} ($n = 1, 2, 3$) sub-problem: Regarding \mathcal{M}_{l_1} , we fix the $\mathcal{M}_{l_2}^{(k)}$, $\mathcal{M}_{l_3}^{(k)}$ and others parameters. The update of \mathcal{M}_{l_1} can be obtained by minimizing the following expression

$$b_{l_1} f^*(\mathbf{M}_{l_1(1)}) + \frac{1}{2} \|\mathcal{M}_{l_1} - \mathbf{Q}_l^{(k+1)} - \mathbf{Z}_{l_1}^{(k)}\|_F^2, \quad (28)$$

where

$$\mathbf{Q}_l^{(k+1)} = \mathbf{c}_l^{(k+1)} \times_1 \mathbf{Q}_{l_1}^{(k+1)} \times_2 \mathbf{Q}_{l_2}^{(k+1)} \times_3 \mathbf{Q}_{l_3}^{(k+1)}. \quad (29)$$

The b_{l_e} can be denoted as $b_{l_e} = \frac{\alpha}{\theta} \prod_{e \neq n} f^*(\mathbf{M}_{l_n(n)})$ and $e = 1, 2, 3$, i.e., b_{l_1} in Eq. (29) can be expressed as

$$b_{l_1} = \frac{\alpha}{\theta} \prod_{n=2,3} f^*(\mathbf{M}_{l_n(n)}).$$

According to Theorem 1 in [29] and Xie's work in [23], Eq. (29) has the following closed-form solution:

$$\mathcal{M}_{l_1}^{(k+1)} = \operatorname{fold}_1(\Psi_{l_1} \Sigma_{d_{l_1}} \Psi_{l_1}^T), \quad (30)$$

where $\Sigma_{d_{l_1}} = \operatorname{diag}(D_{d_{l_1}, \epsilon}(\sigma_1), D_{d_{l_1}, \epsilon}(\sigma_2), \dots, D_{d_{l_1}, \epsilon}(\sigma_M))$ and $\Psi_{l_1} \operatorname{diag}(\sigma_1, \sigma_2, \dots, \sigma_M) \Psi_{l_1}^T$ is the SVD decomposition of $\operatorname{unfold}_1(\mathbf{Q}_l^{(k+1)} + \mathbf{Z}_{l_1}^{(k)})$. Thus, \mathcal{M}_{l_2} and \mathcal{M}_{l_3} can be updated by a similar strategy.

iv) \mathbf{Z}_{l_n} ($n = 1, 2, 3$) sub-problem: From the Eqs. (19), (28) and (29), the \mathbf{Z}_{l_n} can be updated with

$$\mathbf{Z}_{l_n}^{(k+1)} = \mathbf{Z}_{l_n}^{(k)} - (\mathcal{M}_{l_n}^{(k+1)} - \mathbf{Q}_l^{(k+1)}). \quad (31)$$

The all steps in the proposed NLCTF method can be summarized in Algorithm I. Note that the all clusters are constructed by the normalized $\mathcal{X}^{(k+1)}$ not the original $\mathcal{X}^{(k+1)}$. Thus, it is necessary to denormalize the updated $\mathcal{J}_l^{(k+1)}$ ($l = 1, \dots, L$). For the formulation of a low-rank cluster, r_W , r_H and t are set as 6, 6 and 50, respectively. The parameter δ is dependent on λ and $\delta = c\tau^{-1}$, where c is set as the constant 10^{-3} . The size of search window is set as 80×80 in this work.

Algorithm I: NLCTF

Input: $\{\mathbf{y}_s\}_{s=1}^S$, α , τ , θ , μ and other parameters;
1: Initialization: $\{\mathcal{X}^{(0)}\} \leftarrow \mathbf{0}$; $\{\mathcal{X}_l^{(0)}, \mathbf{W}_l^{(0)}\} \leftarrow \mathbf{0}$, initialize $\mathbf{Q}_{l_n}^{(0)}$, $\mathbf{c}_l^{(0)}$ by high-order SVD of $\mathcal{X}_l^{(0)}$; $\{\mathcal{M}_{l_n}^{(0)}, \mathbf{Z}_{l_n}^{(0)}, \mathcal{J}_l^{(0)}\} \leftarrow \mathcal{X}_l^{(0)}$, $\forall n = 1, 2, 3$ and $l = 1, \dots, L$; $k = 0$;
2: **While** not convergence **do**
3: Update $\mathcal{X}^{(k+1)}$ using Eq. (14);
4: Construct all clusters $\mathcal{X}_l^{(k+1)}$ ($l = 1, \dots, L$) using normalized $\mathcal{X}^{(k+1)}$ by employing Eq. (8);
6: for $l = 1:L$
7: Update $\mathbf{c}_l^{(k+1)}$ using Eq. (22);
8: Update $\mathbf{Q}_{l_n}^{(k+1)}$ ($n = 1, 2, 3$) using Eq. (26);
10: Update $\mathcal{M}_{l_n}^{(k+1)}$ ($n = 1, 2, 3$) using Eq. (30);
11: Update $\mathbf{Z}_{l_n}^{(k+1)}$ ($n = 1, 2, 3$) using Eq. (31);
9: Update the denormalized $\mathcal{J}_l^{(k+1)} = \mathbf{c}_l^{(k+1)} \times_1 \mathbf{Q}_{l_1}^{(k+1)} \times_2 \mathbf{Q}_{l_2}^{(k+1)} \times_3 \mathbf{Q}_{l_3}^{(k+1)}$;
10: Update $\mathbf{W}_l^{(k+1)}$ using Eq. (15);
12: End for
13: $k = k + 1$;
14: **End while**
Output: \mathcal{X}

E. Comparison algorithms

To evaluate and compare the performance of our proposed NLCTF algorithm, simultaneous algebraic reconstruction technique (SART), total variation minimization (TV)[8], total

variation and low rank (TV+LR) [10] algorithms, and the newest spatial-spectral cube matching frame method (SSCMF) are chosen and implemented for comparison. It should be emphasized that all hyper-parameters in TV, TV+LR and SSCMF methods are empirically optimized in our experiments.

III. EXPERIMENTS AND RESULTS

In this section, both extensive numerical mouse thorax phantom and injected gold nanoparticles (GNP) mouse real dataset to validate and assess the developed NLCTF algorithm. For the simulation part, we mainly demonstrate the performance of our proposed method in terms of reconstructed image quality, material decomposition accuracy, algorithm convergence, computational cost. To quantitatively evaluate image quality, the root means square error (RMSE), peak-signal-to-noise ratio (PSNR), feature similarity (FSIM) [30] and structural similarity (SSIM) are employed in our numerical experiment. The results from real mouse data furtherly confirm the outperformance of the proposed method in finer structure recovery and image edge preservation with noise reduction.

A. Numerical mouse phantom study

A numerical mouse thorax phantom injected 1.2% iodine concentration is used in this numerical study, as shown in Fig. 2(a), where 1.2% iodine is introduced as the contrast agent. A polychromatic 50KVp x-ray source is employed and the normalized emitted x-ray spectrum is given as Fig. 2 (b). From Fig. 1 (b), it can be seen the spectrum are divided into eight energy bins: [16, 22) keV, [22, 25) keV, [25, 28) keV, [28, 31) keV, [31, 34) keV, [34, 37) keV, [37, 41) keV, [41, 50) keV. The PCD covers 512 pixels and it covers a length of 51.2mm. In this study, the distances starting from x-ray source to PCD and object are set as 180mm and 132mm. The projection views is 640 over a full scan and the radius of field of view (FOV) is 38.4 mm. The noisy projection datasets in Radon space are obtained by a post-logarithmic operation on the received photon numbers. The number of emitted photons for each x-ray path is set as 2×10^4 . The all the reconstructed energy bins images covering an area of 512×512 matrixes are obtained from different reconstruction methods after 50 iterations.

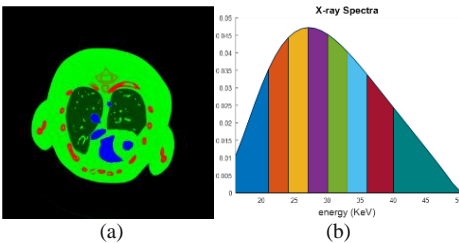


Fig.2 (a) represents the realistic mouse thorax phantom, where green, red and blue stand for water, bone and iodine, respectively. (b) is the normalized x-ray source emitted spectrum.

The parameter selection is a challenging problem for the proposed NLCTF method, where mainly contains four parameters, i.e., α , δ , θ , μ . To make it clear for the parameters selection, these parameters are summarized in the following Table I. The other parameters in competing algorithms are optimized, and their best results are picked up for comparison and analysis.

Table I. NLCTF parameters.

Methods	Dose	α	τ	θ	μ
Simulation study	2×10^4	10	0.050	250	0.5
Real datasets	-	10	0.075	250	0.5

1). Reconstruction results

Fig. 3(a) demonstrates the reconstructed images of three representative energy channels (1st, 4th and 8th), where the reference images are reconstructed from noise-free multi-energy projection by SART. It can be seen that the images reconstructed with the SSCMF method has more finer structures and details compared with those are obtained using TV+LR method followed by TV algorithm. Without no prior knowledge in the mathematical model, there are always strongest noise and image artifacts for the SART results. However, compared with the other competing reconstruction algorithms, the NLCTF method achieves success in capturing smaller image structures and details. This point is further confirmed with the zoomed soft tissue region A in Fig. 4(a). There are abundant details in the extracted region A, most of them (especially for the small features) are covered by the noise for SART results. Compared with TV and TV+LR methods, the SSCMF shows higher quality results. However, the finer structure and details are still lost in the SSCMF results, which are indicated by arrows in Fig. 4(a). In comparison, the NLCTF algorithm can accurately reconstruct most of the small features and details. In addition, Fig. 3(a) also shows the NLCTF method can easily distinguish finer image edge to avoid image structures deblurring, which is determined by the extracted bony region B in Fig. 4(b). Fig. 4(b) demonstrates a zoomed bony region, where thoracic vertebra bones are separated by low-density tissues. It can be seen that the SART results contain severe image noise, especially in the 8th channel where the signal-to-noise ratio (SNR) was so low that the thoracic vertebra bony structures cannot be distinguished from soft tissue. The SSCMF results preserved more bone structures than the TV and TV+LR based techniques. However, the image edge surrounding bone region is still not clear. In contrast, the proposed NLCTF can recover sharp image edge and suppress image noise much better. From Fig. 3(b), one can see that the resultant difference images from the NLCTF method are weaker than those obtained from other competing methods. It means that reconstructed results using the NLCTF algorithm are closer to the ground truth compared with TV, TV+LR and SSCMF algorithms. Fig. 5 plots representative the purple profiles (1st and 8th channels) in bony structure A. It can be observed that the profiles of NLCTF method are closer to the ground truths compared with other competitors.

To quantitatively evaluate and analyze the reconstructed image quality, the values of image assessment indexes are listed in Fig. 6. It shows that the proposed NLCTF can always obtain the smallest RMSEs for all channels, followed by the SSCMF and then TV+LR method which has slightly smaller RMSEs than the TV. In terms of PSNR, the similar conclusions can be obtained. The SSIM and FSIM measure the similarity between reconstructed images and references, they are recently employed to compare CT image quality [18, 31]. Here, the dynamic range of all channel images are scaled to [0 255]. The closer to 1.0 SSIM and FSIM are, the better the reconstructed image quality is. In Fig. 6, NLCTF results obtain the greatest FISM values for all channels, followed by the SSCMF and

TV+LR. Similar to the index of FSIM, the NLCTF has a maximum SSIM value compared with the other four comparisons. In general, NLCTF method has the higher image quality in terms of quantitative assessment.

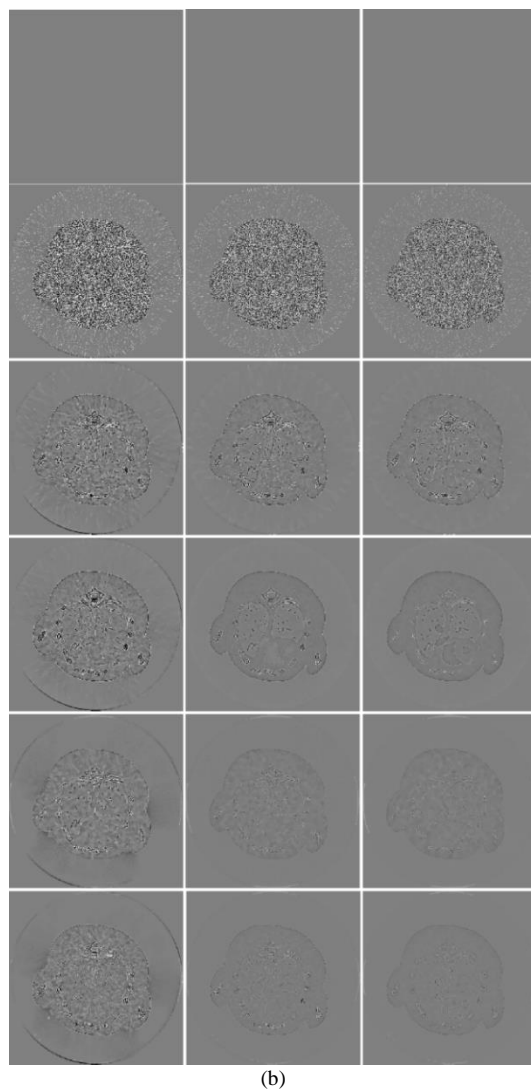
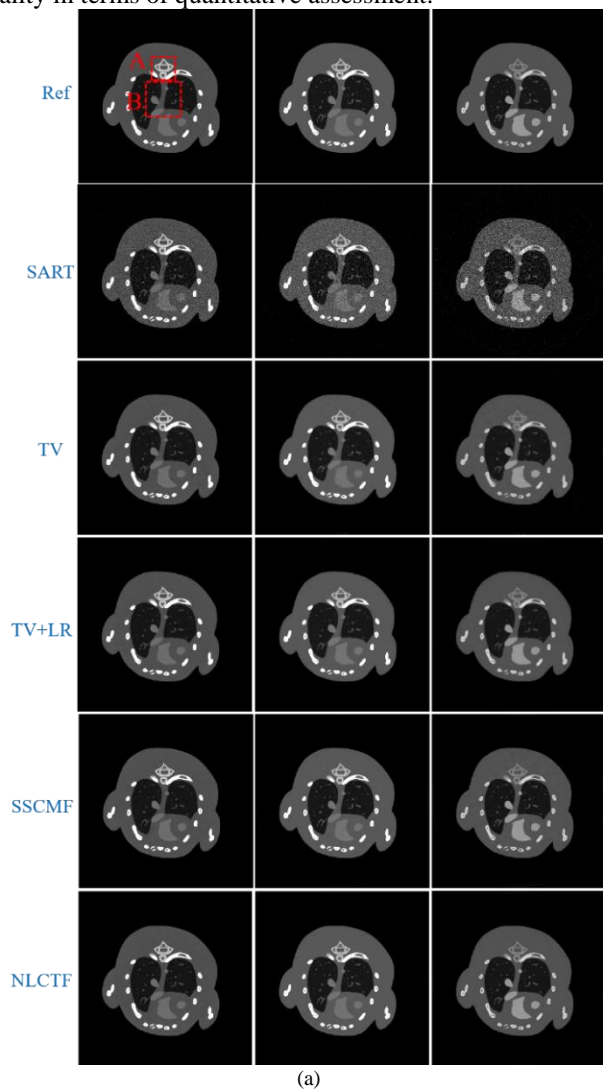


Fig.3 (a) represents three representative energy bine reconstructed results. The 1st to 3rd columns are the 1st, 4th and 8th channels, and their display windows are [0, 3], [0, 1.2] and [0, 0.8] cm^{-1} respectively. (b) is the difference images between the references and reconstructed images and its display is [-0.2, 0.2] cm^{-1} .

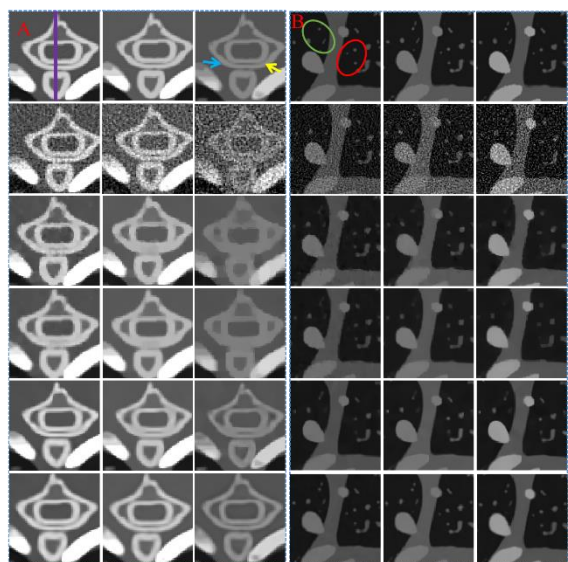


Fig. 4. Magnified ROIs A (bony structure) and B (soft tissue) in Fig. 3(a).
2). Material Decomposition

To evaluate the performance of all reconstructed algorithms in aspect of material decomposition, the reconstructed results are furtherly decomposed into three basis materials (soft tissue, iodine contrast agent and bone) utilizing an post-processing material decomposition method [17]. Fig. 7 shows the three basis materials decomposition results and the merged color images. The first column of Fig. 7 shows bone component, it can be seen that soft tissue and iodine contrast agent are wrongly introduced by the SART. Compared with the SSCMF results, more pixels of the iodine from TV and TV+LR are also wrongly classified into bone structure. In contrast, the NLCTF result has a clear bone map. In terms of the soft-tissue component (2nd column), the proposed NLCTF method can not only provides more finer structures and details, but also recover more sharp edge structure. This can be confirmed with the magnification of bone structure in soft tissue maps. The bone

structure has an impact on accuracy of the iodine contrast agent component, especially the results from SART, TV and TV+LR results. Compared with the results of SSCMF and NLCTF, component map of the later is more clear. To furtherly enhance creditability about the above conclusions, the RMSE values are listed to quantitatively evaluate the accuracy of three basic material decomposition in Table II.

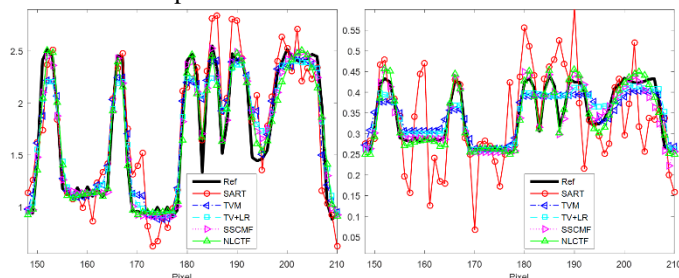


Fig. 5. The profiles from 1st (left) and 8th (right) channels along the purple line in Fig. 4.

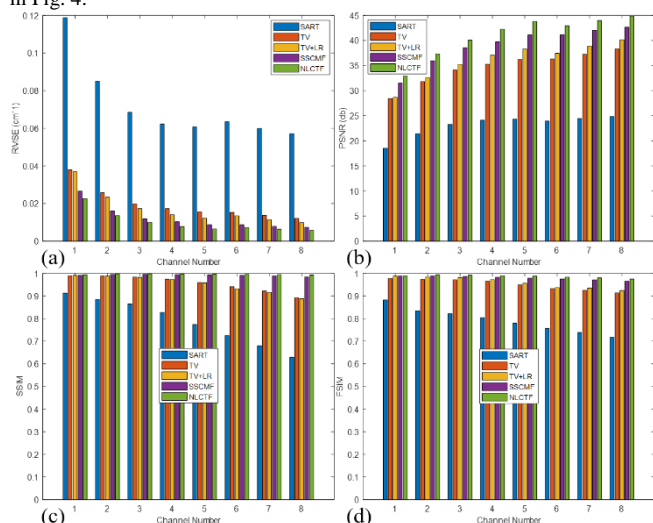


Fig. 6. Quantitative image quality evaluation results.

Table II RMSEs (unit: 10^{-2} cm^{-1}) of three decomposed basic material.

Methods	SART	TV	TV+LR	SSCMF	NLCTF
Bone	1.27	0.70	0.85	0.50	0.47
Soft tissue	6.77	2.61	2.67	1.90	1.62
Iodine	4.96	1.95	1.87	1.19	0.99

3). Convergence analysis and computational cost

There are two regularization terms in KBR model, i.e., sparsity constraint of core tensor and low-rank property of tensor unfolding. In this study, L_0 -norm and nuclear norm are employed to enhance sparsity and low-rank properties respectively, which result in the convergence complicated. In addition, the L_0 -norm minimization of core tensor coefficients is nonconvex optimization problem, which also makes the convergence more difficult. To investigate the performance of NLCTF method in aspect of algorithm convergence, Fig. 8 shows the averaged RMSE and PSNR values among all energy channels vs. iteration number. Since the projection datasets are corrupted by photon noise, the PSNR values of SART increase rapidly and then drop off slowly [7]. It can be seen that RMSEs of all optimization methods are strictly decreasing with iteration number and finally converge to their stable point. Specially, the NLCTF can obtain an optimized solution with a smaller RMSE or a higher PSNR, followed by SSCMF, TV+LR and TV.

Regarding the computational costs, the NLCTF method are divided into two major procedures: data fidelity update and regularization constraint. The backprojection reconstruction step is necessary for all iteration algorithms and different regularization terms correspond to different computational costs. In this study, all the source code are programmed with Matlab (2017b) in PC (8 CPUs @3.40GHz, 32.0GB RAM, Intel(R) HD Graphics 530). The backprojection step is speedup with GPU technique and regularization constraint step is only performed on CPU. Table III lists the consumed time with one iteration for all algorithms.

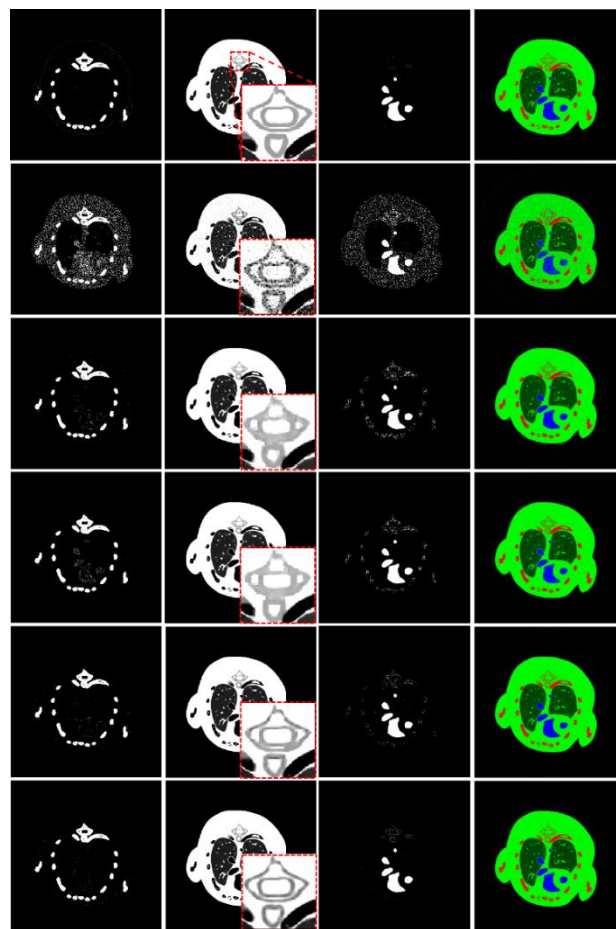


Fig. 7. Three basic materials decomposed from the reconstructed results in Fig. 3(a). The 1st to 3rd columns represent bone, soft tissue and iodine and their display windows are [0, 0.05], [0.2, 0.8] and [0, 0.25] cm^{-1} . The 4th column images are merged images, where red, green and blue represent bone, soft tissue and iodine. The 1st row is the reference and 2nd to 6th rows are reconstructed results using SART, TV, TV+LR, SSCMF and NLCTF methods.

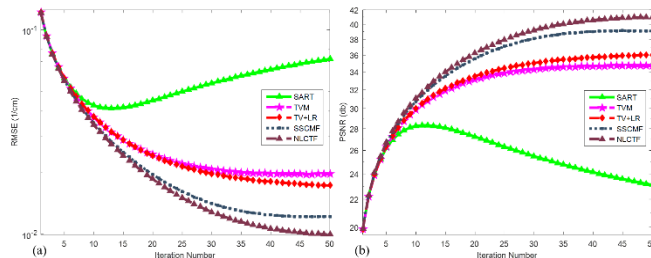


Fig. 8 Convergence curves in terms of RMSEs and PSNRs.

Table III Computational costs of all reconstruction methods.

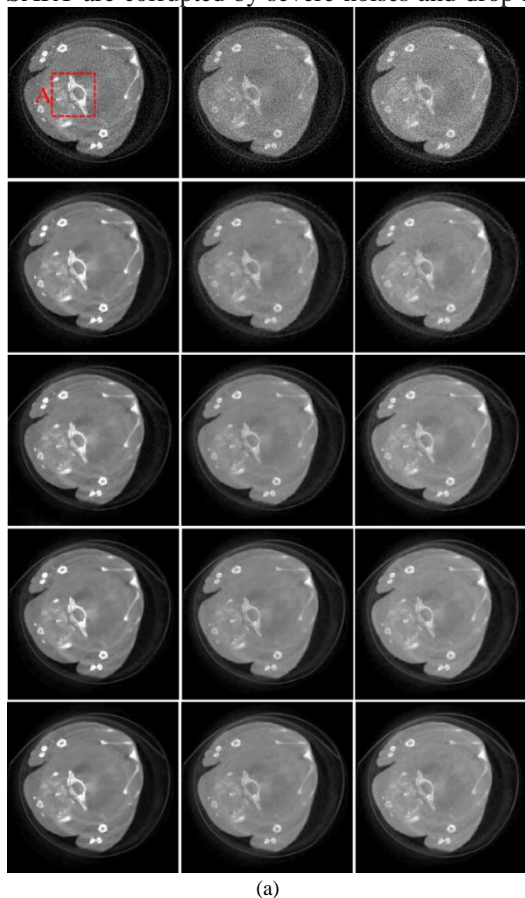
Methods	SART	TV	TV+LR	SSCMF	NLCTF
Data fidelity	114.58	114.58	114.58	114.58	114.58

Regularization	0	1.64	0.52	38.23	327.53
----------------	---	------	------	-------	--------

B. Real mouse experiment

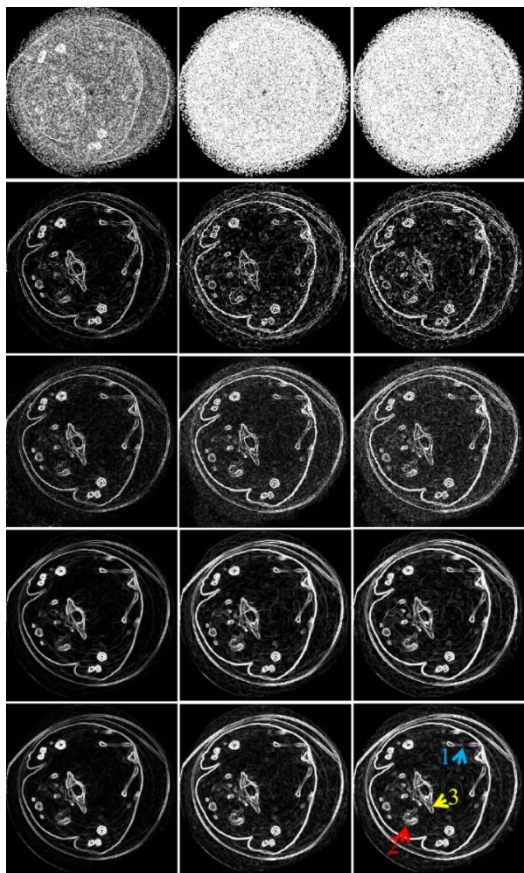
In this study, a mouse was scanned by a MARS micro spectral CT system, whose includes one micro x-ray source and one flat PCD. The distances between the source to the PCD and object are 255 mm and 158 mm respectively. The PCD horizontally includes 512 pixel and its length is 56.32 mm, resulting in a diameter of an FOV with 18.42 mm. The gold nanoparticles (GNP) as contrast agent is introduced into mouse. The projection contains 13 energy channels with 371 views. Note that the PCD only contains two energy bins so that it is necessary to adopt multiple scans to obtain the projections with 13 energy channels. To compare all reconstruction algorithms in practical applications, the projections for the central slice are extracted and employed in this experiment. The size of each reconstructed channel image is 512×512.

Fig. 9(a) and (b) show the reconstructed original and gradient images of four representative energy channels (1st, 9th and 13th). The 1st row of Fig. 9 demonstrate that the images reconstructed by the SART are corrupted by severe noises and drop most of



(a)

details and finer structure. Eventually, it is difficult to distinguish small bone details and soft tissue. The image quality of TV and TV+LR method are improved a lot (2nd and 3rd rows). Both TV and TV+LR models contain TV regularization constraint, which result in the blocky artifacts in their results, especially in soft tissue structures. The SSCMF method has a good performance in recovering finer structures as well as preserving image edges to some extent (4th row) [7]. However, compared with the SSCMF, the proposed NLCTF technique has a stronger ability of edge preserving and feature recovering with noise reduction. For example, the finer bone structure indicated by the arrow “1” are broken in other competitors, but it always stays continuous for the NLCTF results. The shape of bone marked with arrow “2” is slightly distorted in the images reconstructed by the SSCMF technique or even broken in TV, TV+LR and SART results. However, the shape from NLCTF is very clear. The structures of sternum labeled with arrow “3” is hardly observed in all comparisons, but it still can be found in our new method. The extracted bony ROI A is furtherly confirmed the advantages of NLCTF algorithm in Fig. 10.



(b)

Fig. 9. (a) represents the reconstructed original from 1st, 9th and 13th (from left to right) energy bins and (b) is the corresponding gradient images. The 1st to 5th rows are reconstructed results using SART, TV, TV+LR, SSCMF and NLCTF methods. The display window for (a), 4th and 5th-6th columns are [0, 0.8] cm⁻¹, [0, 0.08] cm⁻¹ and [0, 0.04] cm⁻¹ respectively.

IV. CONCLUSIONS AND DISCUSSIONS

To reconstruct high quality spectral images with noisy projections, the NLCTF method was proposed and developed in this work. The advantages are mainly reflected in the following two aspects. First, compared with our recent SSCMF method, the NLCTF explores low-rank property among spatial-

spectrum space by formulating small low-rank-based cube. It not only can achieve higher quality of reconstructed images with more finer features and clear image edge, but also it provides a higher accuracy in terms of material decomposition results, especially in bone and soft tissue decomposition. Second, compared with prior-image-knowledge based methods, the NLCTF can obtain the similar or even better

results. To prove this point, the real mouse reconstructed results using TDL technique are also given in Fig. 12. Those results are

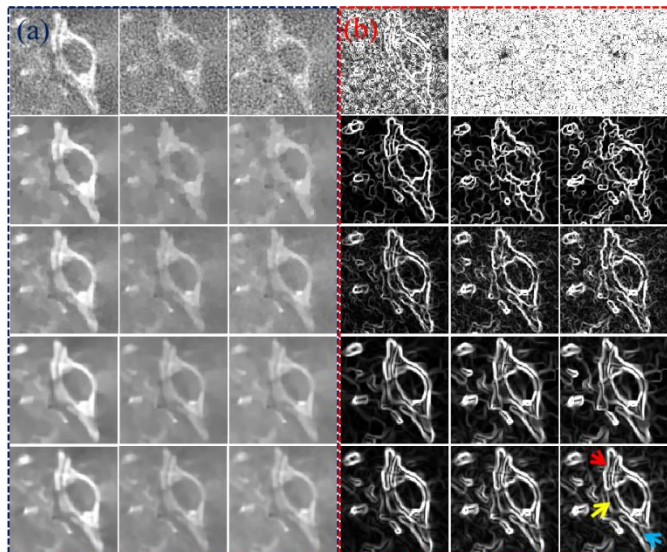


Fig. 10. The magnified bony structure A in Fig. 9 and the 1st-3rd and 4th-6th columns represent the original and gradient images respectively.

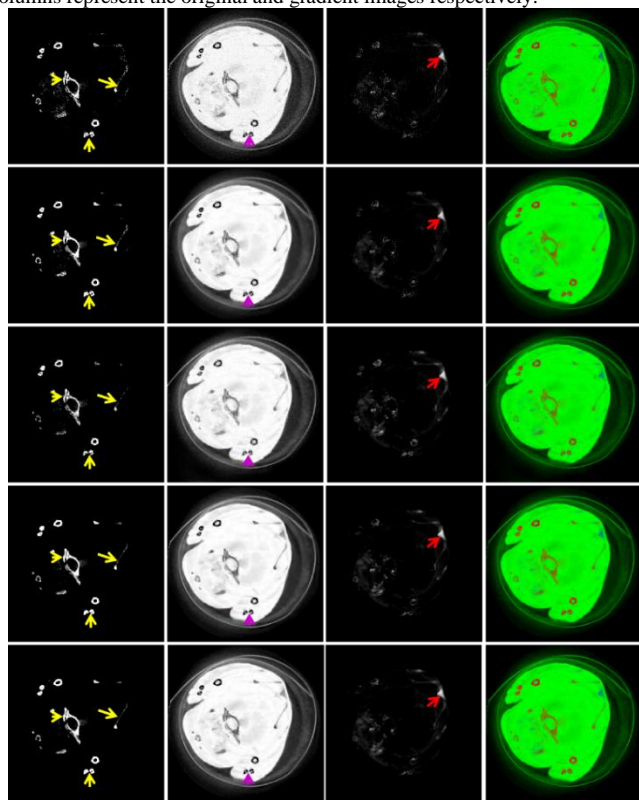


Fig. 11. Three decomposed basic materials of the Fig. 8(a). The 1st to 3th columns represent bone, soft tissue, GNP. The 4th column is the merged color images, where red, green and blue represent bone, soft tissue and GNP. The display windows for the 1st to 3rd columns are [0.1, 0.5], [0, 1] and [0, 0.5] cm⁻¹, respectively.

the same as those given in [17]. From Fig. 12, the small structure marked with red arrows are broken and result in it cannot be observed. However, this structure can be clear observed in our NLCTF results. This point has been analyzed in above sub-section.

The NLCTF algorithm has an outstanding performance in spectral reconstruction, there are some residual problems needs to be solved in practical applications. First, there are parameters

in the NLCTF model which needs to be selected with different imaged objects, such as α , δ , θ , μ , etc. In this study, we only carefully select the optimized parameters by comparing the values of different metrics. However, there may be no reference in practical. In that case, the final result is picked up by our experience, which may lead to an inappropriate result in some cases. Thus, it is important to provide a strategy of selecting a good result by combining the theoretical analysis and contrast experiments in our follow up work. Second, the NLCTF needs larger computational cost than SSCMF, TV+LR and TV. It does make sense to speedup the convergence in practical with GPU technique. Third, the proposed NLCTF is limit to fan-beam projection rather than cone-beam geometry. To generalize it to cone-beam geometry, the 4-order low-rank tensor rather than 3-order cube-based tensor should be formulated.

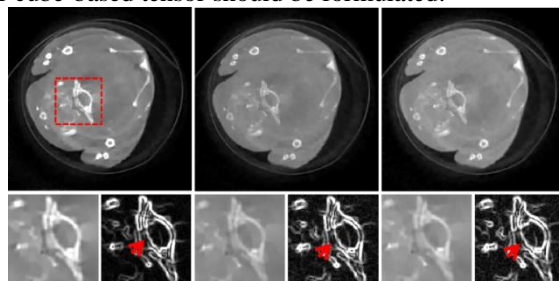


Fig. 12. The first row represents the reconstructed images of three energy channels (1st, 9th and 13th) using TDL technique. The second row shows original and gradient images of the extracted ROI.

To sufficiently explore the similarities among spectrum-spatial space, the Kronecker-Basis-Representation (KBR) measure is employed to decompose the non-local low-rank cube-based tensor in this work. To obtain the optimized solution, the split-Bregman is employed to solve the NLCTF model. Both simulation and real-dataset experiments validate and evaluate the outperformances of our proposed NLCTF reconstruction method. This will be extremely meaningful for spectral CT applications.

REFERENCES

- [1] D. T. Boll *et al.*, "Focal cystic high-attenuation lesions: characterization in renal phantom by using photon-counting spectral CT—improved differentiation of lesion composition," *Radiology*, vol. 254, no. 1, pp. 270-276, 2009.
- [2] W. P. Shuman *et al.*, "Dual-energy liver CT: effect of monochromatic imaging on lesion detection, conspicuity, and contrast-to-noise ratio of hypervascular lesions on late arterial phase," *American Journal of Roentgenology*, vol. 203, no. 3, pp. 601-606, 2014.
- [3] Y. Long and J. A. Fessler, "Multi-material decomposition using statistical image reconstruction for spectral CT," *IEEE transactions on medical imaging*, vol. 33, no. 8, pp. 1614-1626, 2014.
- [4] A. C. Silva, B. G. Morse, A. K. Hara, R. G. Paden, N. Hongo, and W. Pavlicek, "Dual-energy (spectral) CT: applications in abdominal imaging," *Radiographics*, vol. 31, no. 4, pp. 1031-1046, 2011.
- [5] M. Walsh *et al.*, "First CT using Medipix3 and the MARS-CT-3 spectral scanner," *Journal of Instrumentation*, vol. 6, no. 01, p. C01095, 2011.
- [6] K. Taguchi, K. Stierstorfer, C. Polster, O. Lee, and S. Kappler, "Spatio-energetic cross-talk in photon counting detectors: N×N binning and sub-pixel masking," in *Medical Imaging 2018: Physics of Medical Imaging*, 2018, vol. 10573, p. 105734X: International Society for Optics and Photonics.
- [7] W. Wu, Y. Zhang, Q. Wang, F. Liu, Q. Wang, and H. Yu, "Spatial-Spectral Cube Matching Frame for Spectral CT Reconstruction," *inverse problems*, vol. IP-101766.R2, 2018.

- [8] Q. Xu *et al.*, "Image reconstruction for hybrid true-color micro-CT," *IEEE transactions on biomedical engineering*, vol. 59, no. 6, pp. 1711-1719, 2012.
- [9] O. Semerci, N. Hao, M. E. Kilmer, and E. L. Miller, "Tensor-based formulation and nuclear norm regularization for multienergy computed tomography," *IEEE Transactions on Image Processing*, vol. 23, no. 4, pp. 1678-1693, 2014.
- [10] J. Chu, L. Li, Z. Chen, G. Wang, and H. Gao, "Multi-energy CT reconstruction based on low rank and sparsity with the split-bregman method (MLRSS)," in *Nuclear Science Symposium and Medical Imaging Conference (NSS/MIC), 2012 IEEE*, 2012, pp. 2411-2414: IEEE.
- [11] B. Zhao, H. Gao, H. Ding, and S. Molloy, "Tight-frame based iterative image reconstruction for spectral breast CT," *Medical Physics*, vol. 40, no. 3, p. 031905, 2013.
- [12] D. S. Rigie and P. J. L. Rivière, "Joint Reconstruction of Multi-channel, Spectral CT Data via Constrained Total Nuclear Variation Minimization," *Physics in Medicine & Biology*, vol. 60, no. 5, pp. 1741-62, 2015.
- [13] K. Kim *et al.*, "Sparse-View Spectral CT Reconstruction Using Spectral Patch-Based Low-Rank Penalty," *IEEE Transactions on Medical Imaging*, vol. 34, no. 3, pp. 748-760, 2015.
- [14] O. Semerci, N. Hao, M. E. Kilmer, and E. L. Miller, "Tensor-Based Formulation and Nuclear Norm Regularization for Multienergy Computed Tomography," *IEEE Transactions on Image Processing*, vol. 23, no. 4, pp. 1678-93, 2014.
- [15] D. Zeng *et al.*, "Penalized weighted least-squares approach for multienergy computed tomography image reconstruction via structure tensor total variation regularization," *Computerized Medical Imaging and Graphics*, vol. 53, pp. 19-29, 2016.
- [16] B. Zhao, H. Ding, Y. Lu, G. Wang, J. Zhao, and S. Molloy, "Dual-dictionary learning-based iterative image reconstruction for spectral computed tomography application," *Physics in medicine and biology*, vol. 57, no. 24, p. 8217, 2012.
- [17] Y. Zhang, X. Mou, G. Wang, and H. Yu, "Tensor-based dictionary learning for spectral CT reconstruction," *IEEE transactions on medical imaging*, vol. 36, no. 1, pp. 142-154, 2017.
- [18] W. Wu, Y. Zhang, Q. Wang, F. Liu, P. Chen, and H. Yu, "Low-dose spectral CT reconstruction using L0 image gradient and tensor dictionary," *arXiv preprint arXiv:1801.01452*, 2017.
- [19] Z. Yu, S. Leng, Z. Li, and C. H. McCollough, "Spectral prior image constrained compressed sensing (spectral PICCS) for photon-counting computed tomography," *Physics in Medicine & Biology*, vol. 61, no. 18, p. 6707, 2016.
- [20] Y. Zhang, Y. Xi, Q. Yang, W. Cong, J. Zhou, and G. Wang, "Spectral CT reconstruction with image sparsity and spectral mean," *IEEE Transactions on Computational Imaging*, vol. 2, no. 4, pp. 510-523, 2016.
- [21] L. R. Tucker, "Some mathematical notes on three-mode factor analysis," *Psychometrika*, vol. 31, no. 3, pp. 279-311, 1966.
- [22] T. G. Kolda and B. W. Bader, "Tensor decompositions and applications," *SIAM review*, vol. 51, no. 3, pp. 455-500, 2009.
- [23] Q. Xie, Q. Zhao, D. Meng, and Z. Xu, "Kronecker-Basis-Representation based tensor sparsity and its Applications to tensor recovery," *IEEE transactions on pattern analysis and machine intelligence*, 2017.
- [24] Q. Xie *et al.*, "Multispectral images denoising by intrinsic tensor sparsity regularization," in *Proceedings of the IEEE Conference on Computer Vision and Pattern Recognition*, 2016, pp. 1692-1700.
- [25] Y. Wang, D. Meng, and M. Yuan, "Sparse recovery: from vectors to tensors," *National Science Review*, 2017.
- [26] D. Zeng *et al.*, "Low-Dose Dynamic Cerebral Perfusion Computed Tomography Reconstruction via Kronecker-Basis-Representation Tensor Sparsity Regularization," *IEEE transactions on medical imaging*, vol. 36, no. 12, pp. 2546-2556, 2017.
- [27] A. H. Andersen and A. C. Kak, "Simultaneous algebraic reconstruction technique (SART): a superior implementation of the ART algorithm," *Ultrasonic imaging*, vol. 6, no. 1, pp. 81-94, 1984.
- [28] P. Gong, C. Zhang, Z. Lu, J. Huang, and J. Ye, "A general iterative shrinkage and thresholding algorithm for non-convex regularized optimization problems," in *International Conference on Machine Learning*, 2013, pp. 37-45.
- [29] C. Lu, C. Zhu, C. Xu, S. Yan, and Z. Lin, "Generalized Singular Value Thresholding," in *AAAI*, 2015, pp. 1805-1811.
- [30] L. Zhang, L. Zhang, X. Mou, and D. Zhang, "FSIM: A feature similarity index for image quality assessment," *IEEE transactions on Image Processing*, vol. 20, no. 8, pp. 2378-2386, 2011.
- [31] S. Tan *et al.*, "Tensor-based dictionary learning for dynamic tomographic reconstruction," *Physics in Medicine & Biology*, vol. 60, no. 7, p. 2803, 2015.